He II Ly alpha transmission spikes and absorption troughs in eight high-resolution spectra probing the end of He II reionization

Makan, K.; Worseck, G.; Davies, F.B.; Hennawi, J.F.; Prochaska, J.X.; Richter, P.

The Astrophysical Journal, 927:175 (13pp), 2022 March 10 https://doi.org/10.3847/1538-4357/ac524a

He II Lyα Transmission Spikes and Absorption Troughs in Eight High-resolution Spectra Probing the End of He II Reionization

Kirill Makan[1], Gábor Worseck[1], Frederick B. Davies[2], Joseph F. Hennawi[3,4], J. Xavier Prochaska[5,6], and Philipp Richter[1]
[1] Institut für Physik und Astronomie, Universität Potsdam, Karl-Liebknecht-Str. 24/25, D-14476 Potsdam, Germany; kmakan@astro.physik.uni-potsdam.de
[2] Max-Planck-Institut für Astronomie, Königstuhl 17, D-69117 Heidelberg, Germany
[3] Department of Physics, University of California, Santa Barbara, CA 93106-9530, USA
[4] Leiden Observatory, Leiden University, Niels Bohrweg 2, NL-2333 CA Leiden, The Netherlands
[5] University of California Observatories, Lick Observatory, University of California, Santa Cruz, CA 95064, USA
[6] Kavli Institute for the Physics and Mathematics of the Universe (WPI), UTIAS, The University of Tokyo, Kashiwa, Chiba 277-8583, Japan
Received 2021 December 14; revised 2022 February 3; accepted 2022 February 3; published 2022 March 14

Abstract

We present statistics of He II Lyα transmission spikes and large-scale absorption troughs using archival high-resolution ($R = \lambda/\Delta\lambda \simeq 12{,}500$–$18{,}000$) far-UV spectra of eight He II-transparent quasars obtained with the Cosmic Origins Spectrograph on the Hubble Space Telescope. The sample covers the redshift range $2.5 \lesssim z \lesssim 3.8$, thereby probing the rapidly evolving He II absorption at the end of He II reionization epoch. The measured lengths of the troughs decrease dramatically from $L \gtrsim 100$ cMpc at $z > 3$ to $L \simeq 30$ cMpc at $z \sim 2.7$, signaling a significant progression of He II reionization at these redshifts. Furthermore, unexpectedly long $L \sim 65$ cMpc troughs detected at $z \simeq 2.9$ suggest that the UV background fluctuates at larger scales than predicted by current models. By comparing the measured incidence of transmission spikes to predictions from forward-modeled mock spectra created from the outputs of a $(146\ \mathrm{cMpc})^3$ optically thin Nyx hydrodynamical simulation employing different UV background models, we infer the redshift evolution of the He II photoionization rate $\Gamma_{\mathrm{He\,II}}(z)$. The photoionization rate decreases with increasing redshift from $\simeq 4.6 \times 10^{-15}\ \mathrm{s}^{-1}$ at $z \simeq 2.6$ to $\simeq 1.2 \times 10^{-15}\ \mathrm{s}^{-1}$ at $z \simeq 3.2$, in agreement with previous inferences from the He II effective optical depth, and following expected trends of current models of a fluctuating He II-ionizing background.

Unified Astronomy Thesaurus concepts: Cosmic background radiation (317); Hubble Space Telescope (761); Intergalactic medium (813); Quasar absorption line spectroscopy (1317); Reionization (1383); Ultraviolet astronomy (1736)

1. Introduction

The reionization of intergalactic primordial gas completed separately for hydrogen and helium. For hydrogen, several observational tracers, such as the cosmic microwave background (Planck Collaboration et al. 2020), Lyα emitters (e.g., Mason et al. 2018; Hu et al. 2019), and Lyman series absorption (e.g., Fan et al. 2006), suggest that hydrogen reionization ended at $z \sim 6$ or even somewhat later (e.g., Becker et al. 2015; Kulkarni et al. 2019a; Choudhury et al. 2021). Due to their similar ionization potential, hydrogen and He I were reionized by soft UV photons that were likely emitted by star-forming galaxies (e.g., Madau et al. 1999; Faucher-Giguère et al. 2008; Eide et al. 2020). He II reionization, however, requires hard UV photons ($E \geqslant 54.4$ eV) from quasars and was completed later at $z \sim 3$ (e.g., Madau & Meiksin 1994; Fardal et al. 1998; Miralda-Escudé et al. 2000; Sokasian et al. 2002; Furlanetto & Oh 2008; McQuinn et al. 2009; Compostella et al. 2013, 2014; La Plante et al. 2017; Kulkarni et al. 2019a). The progression of He II reionization determines the time evolution and spatial variance in the intergalactic UV radiation field (e.g., Furlanetto & Dixon 2010; Davies et al. 2017; Meiksin 2020), and thus, is a crucial probe of observational cosmology.

Depending on the employed parameters such as the quasar luminosity function and spectral energy distribution, the current hydrodynamical simulations result in a broad range of He II reionization histories ending at $2.3 \lesssim z \lesssim 3.4$ (Compostella et al. 2013, 2014; La Plante et al. 2017). Primarily, these simulations were used to predict the redshift evolution of the intergalactic medium (IGM) temperature as inferred from the H I Lyα forest (e.g., Boera et al. 2014; Hiss et al. 2018; Walther et al. 2019).

In principle, He II Lyman series absorption can be observed in the far-UV (FUV) against $z > 2$ quasars (e.g., Miralda-Escude 1993; Jakobsen et al. 1994; Madau & Meiksin 1994). In practice, however, cumulative intergalactic H I Lyman continuum absorption and the rapidly declining $z > 3$ quasar luminosity function strongly limit the number of quasars with FUV emission at the He II Lyα rest-frame wavelength $\lambda_\alpha = 303.7822$ Å (Møller & Jakobsen 1990; Picard & Jakobsen 1993; Worseck & Prochaska 2011). Statistical He II absorption studies toward >20 quasars were enabled only recently with preselection of FUV-bright quasars from Galaxy Evolution Explorer (GALEX; Morrissey et al. 2007) photometry (Syphers et al. 2009a, 2009b; Worseck & Prochaska 2011) and spectroscopic follow-up with the FUV-sensitive Cosmic Origins Spectrograph (COS) on board the Hubble Space Telescope (HST; Worseck et al. 2011, 2016, 2019; Syphers et al. 2012).

One of the simplest He II absorption statistics is the He II Lyα effective optical depth $\tau_{\mathrm{eff}} = -\ln\langle e^{-\tau_\alpha}\rangle_{\Delta z}$ over a predefined redshift interval Δz. In the current sample of 25 He II sight lines, the variance of τ_{eff} is in agreement with IGM

density fluctuations in a uniform UV background at $z \lesssim 2.7$, indicating the end of the He II reionization epoch (Worseck et al. 2019, hereafter W19). However, at higher redshifts ($2.7 \lesssim z \lesssim 3.2$), the much larger sight-line-to-sight-line variance of $\tau_{\rm eff}$ requires a fluctuating UV background (Davies et al. 2017) at still very low He II fractions of $\sim$1% (Worseck et al. 2016; Davies et al. 2017; W19). Because the $\tau_{\rm eff}$ statistic is readily applicable to the available statistically useful sample of low-quality low-resolution He II spectra it remains the most direct observational probe of the He II reionization epoch, analogous to H I at $z \gtrsim 5.5$ (e.g., Fan et al. 2006; Eilers et al. 2019; Bosman et al. 2021).

Alternative approaches, such as statistics of transmission spikes (Gallerani et al. 2006, 2008; Barnett et al. 2017; Gnedin et al. 2017; Chardin et al. 2018; Garaldi et al. 2019; Gaikwad et al. 2020; Yang et al. 2020) and troughs between them (Songaila & Cowie 2002; Paschos & Norman 2005; Fan et al. 2006; Gallerani et al. 2006, 2008; Gnedin et al. 2017; Zhu et al. 2021), have already been used to probe the end of the H I reionization epoch. The same statistics may also distinguish between different He II reionization models (Compostella et al. 2013). However, so far they have been applied to only two $z > 3.1$ He II sight lines with the required high-resolution data (Makan et al. 2021; hereafter M21).

Here, we present statistics of He II Lyα transmission spikes and troughs in the high-resolution (R = 12,500–18,000) HST/COS spectra of eight He II-transparent quasars covering $2.5 \lesssim z \lesssim 3.8$. By employing the automated transmission spike measurement technique presented in (M21), we aim to probe the end of the He II reionization epoch, providing an alternative approach to inferences from $\tau_{\rm eff}$. This paper is structured as follows. In Section 2, we describe our sample and our custom data reduction. In Section 3, we explain and apply our measurement technique for transmission spikes and troughs. We compare the measured incidence of transmission spikes to predictions from photoionization models to infer the redshift-dependent He II photoionization rate $\Gamma_{\rm He\,II}(z)$ in Section 4. Finally, we summarize in Section 5. We use a flat cold dark matter cosmology with dimensionless Hubble constant $h = 0.685$ ($H_0 = 100h\,{\rm km\,s^{-1}\,Mpc^{-1}}$) and density parameters ($\Omega_{\rm m}$, $\Omega_{\rm b}$, Ω_Λ) = (0.3, 0.047, 0.7), consistent with Planck Collaboration et al. (2020).

2. High-resolution HST/COS Spectra of He II-transparent Quasars

2.1. Archival HST/COS Data

Our sample of He II-transparent quasars with high-resolution HST/COS (Green et al. 2012) G130M spectra includes eight objects with $z_{\rm em} = 2.74$–3.81 (Table 1). The two quasars at $z_{\rm em} > 3.5$ were recently observed in HST Cycle 25 Program 15356 at COS Lifetime Position (LP) 4 and studied in M21. Exposures taken at several central wavelengths ensured a gap-free coverage from 1067–1473 Å at a wavelength-dependent resolving power of $R = 14{,}000$ at 1250 Å. We complemented these data with archival HST high-resolution spectra of six lower-redshift He II-transparent quasars. HE 2347−4342, one of the FUV-brightest He II-transparent quasars, was observed in Program 11528 at LP 1 providing $R \simeq 18{,}000$ at 1250 Å (Shull et al. 2010). It was later reobserved in Program 13301 at LP 2 with the short-wavelength setup centered at 1222 Å along with HS 1700+6416 (Shull & Danforth 2020). The same 1222 Å setup was used for the quasars HS 1024+1849, Q1602+576, and HS 0911+4809 in Program 12816 (PI: D. Syphers). Finally, Q0302−003 was observed with COS in Program 12033 at LP 1 with the central wavelength settings 1291 and 1318 Å (Syphers & Shull 2014).

2.2. Data Reduction

All data were reduced following M21 by using `CALCOS` v3.3.9 along with our improved FUV data reduction pipeline `FaintCOS`[7] v1.0, which has been extensively described and tested in M21. `FaintCOS` is the only publicly available pipeline that enables accurate dark current subtraction and coaddition of subexposures of faint objects taken in the Poisson regime at the sensitivity limit of HST/COS. We adjusted the reduction parameters in `FaintCOS` for every object individually to account, among other things, for the detector degradation and changing observing conditions.

For some quasars, the data were obtained at different epochs and thus require a flux scaling to account for potential quasar variability and varying sensitivity of the COS detector. For instance, the flux of HE 2347−4342 decreased by $\sim$10% between 2009 November and 2014 August. Furthermore, the data set from 2014 August of this particular sight line showed an abrupt change in continuum flux between FUV detector segment A and B owing to the changed high-voltage settings on the latter. We used the low-resolution G140L HST/COS data (Program 13301) to rescale the individual exposures. On the other hand, the rescaling for HS 1700+6416 was not required because the relative flux difference between 2014 April and 2014 December, although taken at different high-voltage levels, remained <2%, which is in agreement with the HST/COS absolute flux calibration accuracy of 5%.

The single exposure spectra were coadded and rebinned in count space to Nyquist-sampled spectra with 0.04 Å pixel^{-1} (0.03 Å pixel^{-1} for Q0302−003), preserving the Poisson distributed counts. Q0302−003 has a different binning due to the higher spectral resolution R = 18,000 at 1250 Å (R = 12,500–14,500 for other data). A comparison of the individual exposures (and visits for the faintest objects) did not reveal any systematic wavelength calibration differences, preserving the spectral resolution for He II transmission spikes. The flux calibration curves and flat fields of individual exposures determined by `CALCOS` were combined using the pixel exposure time weighted average.

We suppressed the contamination by geocoronal emission lines (N I λ1134, N I λ1168, N I λ1200, H I λ1216, N I λ1243, O I λ1304, O I λ1356) by replacing the affected spectral regions with the data taken during orbital night (Sun altitude $\leqslant 0°$). We were able to remove all geocoronal emission, except Lyα, along most of our sight lines in the He II Lyα absorption region of the spectra. Q0302−003 and HS 0911+4809 contain obvious residuals of N I λ1134, N I λ1200, and O I λ1304. Spectral regions with residual contamination are excluded from the analysis. All interstellar medium H_2 fluorescence lines are considered to be negligible, because even the strongest lines are not present in the predominantly saturated spectra of HE2QS J2311−1417 and HE2QS J1630+0435 (M21). The weak diffuse UV sky background $f_{\rm sky}$ was subtracted by using GALEX data (Murthy 2014) following the procedure by Worseck et al. (2016).

We calculated the asymmetric statistical errors of the background-subtracted flux in the Poisson regime at 68.27% confidence level using the method by Feldman & Cousins (1998). The resulting signal-to-noise ratio (S/N) is 3–28 per

[7] https://github.com/kimakan/FaintCOS

Table 1
Sample of the He II-Transparent Quasars Observed with HST/COS G130M

Object	R.A. (J2000)	Decl. (J2000)	z_{em}[a]	t_{exp}(s)	S/N[b]	R[c]	$\Delta\lambda$(Å)	PID[d]	$f_{1500\ Å}$[e]	α[f]	z_{abs}	$\log N_{H\,I}$[g]
HS 1700+6416	$17^h01^m00^s.61$	+64°12′09.″1	2.7472	59,547	20	12,500	1060–1370	13301	1.8836	−2.027	0.8642	16.09
											0.7217	16.23
											0.5523	15.77
HS 1024+1849	$10^h27^m34^s.13$	+18°34′27.″6	2.8521	28,689	5	12,500	1060–1370	12816	3.224	−0.732	...	...
Q1602+576	$16^h03^m55^s.93$	+57°30′54.″4	2.8608	15,613	7	12,500	1060–1370	12816	6.019	−2.701	...	...
HE 2347−4342	$23^h50^m34^s.23$	−43°25′59.″8	2.8852	28,455	28	14,500	1060–1444	11528	17.424	−2.520	...	...
				41,392				13301			...	...
Q0302−003	$03^h04^m49^s.86$	−00°08′13.″5	3.2850	24,869	5	18,000	1125–1465	12033	2.879	−3.534	...	...
HS 0911+4809	$09^h15^m10^s.01$	+47°56′58.″8	3.350	26,863	6	12,500	1060–1370	12816	3.163	−0.572	...	...
HE2QS J2311−1417	$23^h11^m45^s.46$	−14°17′52.″2	3.700*	54,920	3	14,000	1080–1473	15356	2.065	−2.600	0.7515	16.37
											0.4779	<17.2
HE2QS J1630+0435	$16^h30^m56^s.33$	+04°35′59.″4	3.810*	45,915	3	14,000	1080–1473	15356	2.955	−1.158	...	...

Notes.
[a] Redshift reference: Worseck et al. (2021). The two sight lines indicated with * are from Khrykin et al. (2019).
[b] Poisson S/N per pixel of the coadded spectrum in the continuum near the He II Lyα in the quasar rest frame.
[c] Resolving power $R = \Delta\lambda/\lambda$ at 1250 Å.
[d] HST program number.
[e] Continuum flux density at 1500 Å in 10^{-16} erg cm^{-2} s^{-1} Å^{-1}.
[f] Power-law spectral index α for $E_\lambda = f_{1500\ Å}(\lambda/1500\ Å)^\alpha$.
[g] Logarithmic column density of identified intervening H I absorber at z_{abs} in cm^{-2}.

pixel near He II Lyα in the quasar continuum. The S/N varies greatly between the sight lines owing to the different exposure times and quasar brightness. The reduced spectra were corrected for Galactic extinction by applying the extinction curve A_λ from Cardelli et al. (1989). For the correction, we used the line-of-sight selective extinction from Schlegel et al. (1998) and assumed the Galactic average ratio between the total V-band extinction and selective extinction $R_V = 3.1$.

As in W19 and M21, we used low-resolution COS and STIS G140L spectra to define quasar power-law continua $E_\lambda \propto \lambda^\alpha$. For this, absorption-free regions in the quasar continuum were manually selected and fitted using the maximum likelihood method. Additionally, we determined the redshifts of partial Lyman limit systems through their Lyman series absorption lines and added their H I column densities as free parameters to the power-law fit. The resulting continua were scaled to the high-resolution G130M data using the overlapping quasar continua redward of He II Lyα. The results are listed in Table 1 along with the identified partial Lyman limit systems.

2.3. General Overview of the Spectra

Figure 1 shows the high-resolution HST/COS G130M spectra of our eight quasars (undersampled for visualization) along with their respective fitted and scaled continua. The substantial decrease in S/N at $\lambda < 1120$ Å is due to the decreasing sensitivity of the detector at these wavelengths, while the extended scatter at 1280 Å in the spectra of the two $z_{em} > 3.5$ quasars is due to the short exposure time resulting from partial overlap of multiple central wavelength settings.

Blueward of He II Lyα in the quasar rest frame we observe predominant intergalactic He II Lyα absorption. Enhanced ionization around the background quasar is visible as excess transmission in its proximity zone (Khrykin et al. 2019; Worseck et al. 2021). Noticeably, the He II Lyα absorption is predominantly saturated at $z > 3$, but showing occasional transmission spikes (e.g., at $z \sim 3.17$ toward HS 0911+4809 and at $z \sim 3.58$ toward HE2QS J1630+0435). In contrast at lower redshifts (e.g., $z \lesssim 2.7$ toward HE 2347−4342), there is already a lot of small-scale structure that resembles an emerging He II Lyα forest. Three of the spectra also cover intergalactic He II Lyβ, discussed for the two $z > 3.5$ quasars in M21.

3. Observed He II Transmission Features

3.1. Measurement Technique

Transmission spikes were detected and fitted with our fully automated spike finding code presented in M21. The algorithm decomposes the spectrum into a series of Gaussian transmission spikes. Obviously, absorption features cannot be modeled as emission features, but our approach allows for a fast one-to-one analysis of predominantly saturated spectra. Here, we also perform measurements of the troughs to obtain an additional statistic of He II reionization (e.g., Compostella et al. 2013).

In short, we used the Poisson probability

$$P(>N|B) = 1 - \sum_{k=0}^{N} \frac{B^k e^{-B}}{k!} \quad (1)$$

for N Poisson counts given the background B as a 9 pixel (0.27–0.36 Å) running average to define spectral regions with significant ($P(>N|B) < 0.0014$, 3σ) transmission. In order to reliably fit Gaussian profiles to the individual transmission spikes even in low S/N spectra at $z > 3$, we required that a significantly transmitting region must have at least nine consecutive $P <$ 0.0014 pixels. After smoothing of the transmission with a Gaussian filter ($\sigma_f = 0.1$ Å), individual spikes were found by counting all transmission maxima in these spectral regions. Following M21, our primary statistic for transmission spikes is their incidence, i.e., number of maxima in predefined redshift bins. All our measurements were carried out in the valid spectral regions which exclude the He II Lyα proximity zone (Khrykin

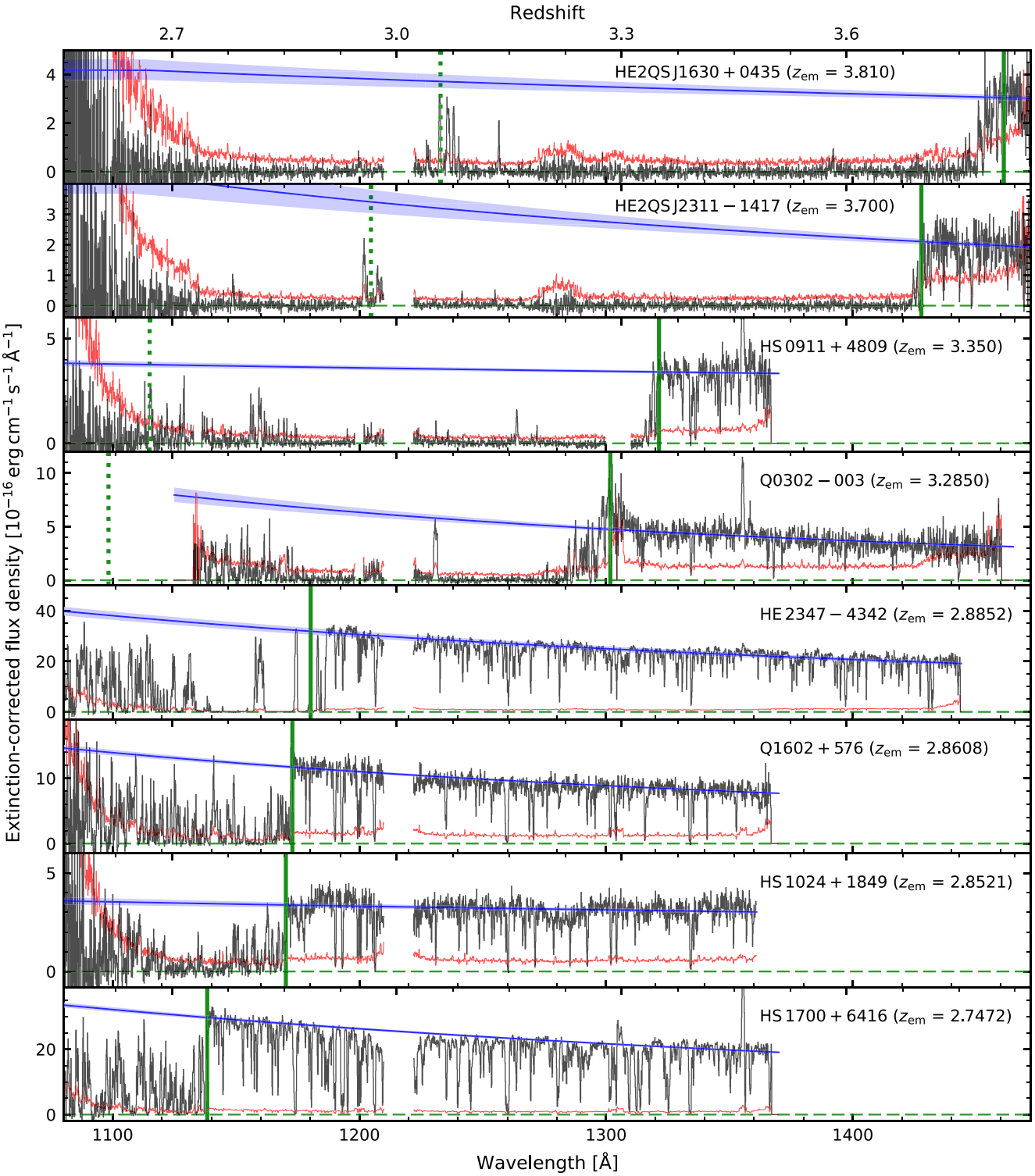

Figure 1. HST/COS G130M spectra (black) and their corresponding Poisson single-sided upper error (84.13% confidence level, red) of eight He II-transparent quasars sampled at 0.12 Å pixel^{-1} for visualization. The strong geocoronal H I Lyα emission line in all spectra, as well as the geocoronal O I in the spectrum of HS 0911+4809, is omitted. The green lines indicate He II Lyα at the redshift of the quasars with the quasar continuum redward of it. The reduced flux at ∼1205 and ∼1225 Å in the quasar continua are the damping wings of the Galactic H I Lyα absorption. The green dotted lines mark He II Lyβ. The fitted continua from HST low-resolution spectra and the corresponding 1σ error are shown in blue.

et al. 2019; Worseck et al. 2021), the overlapping He II Lyβ forest, regions contaminated by geocoronal emission lines, and regions of very low sensitivity resulting in $P > 0.0014$ even at full transmission ($\tau_\alpha = 0$).

We defined spectral regions between transmission spikes as troughs. These regions do not contain significant small-scale transmission given our data quality. For every trough, we measured the length L and the effective optical depth $\tau_{\rm eff}$. Our

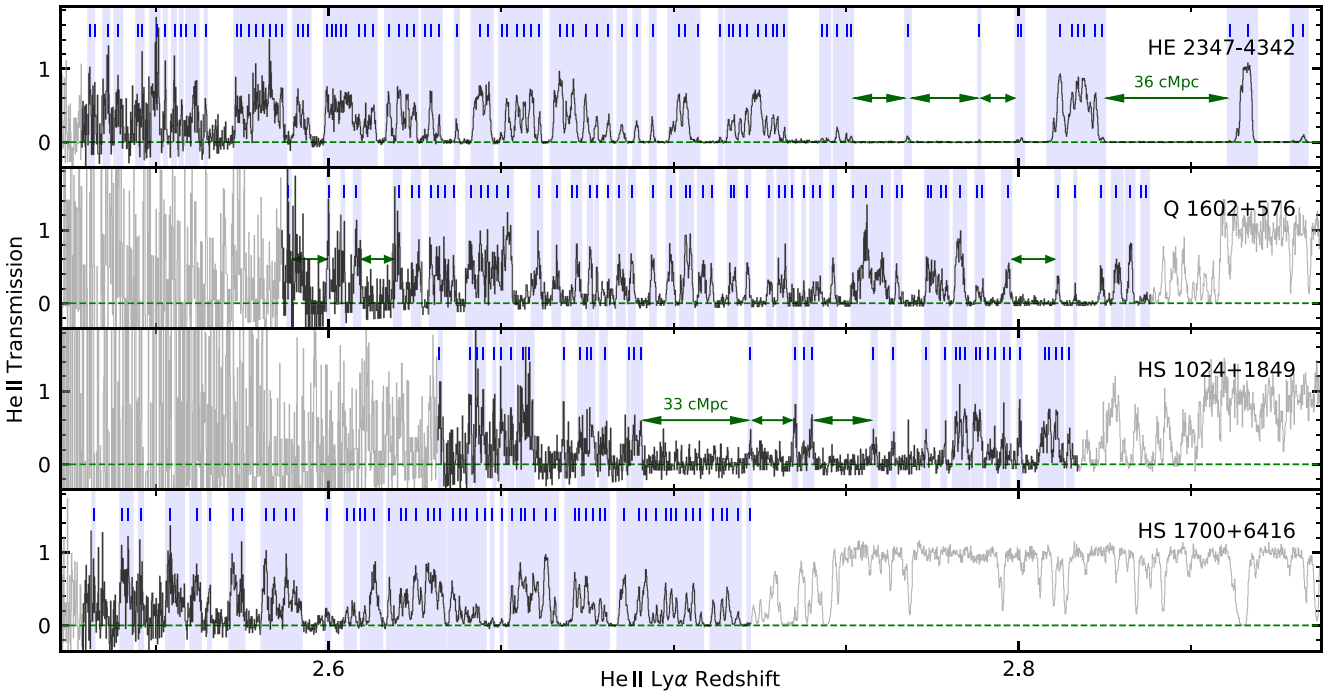

Figure 2. Detected He II Lyα transmission spikes and troughs at the original spectral binning of 0.04 Å toward the four $z_{\rm em} < 2.9$ quasars. The spectral regions plotted in gray are omitted from the analysis due to the low sensitivity at the short-wavelength end of the spectrum, and due to the onset of the He II Lyα proximity zone at the long-wavelength end. Blue-shaded areas indicate spectral regions with significant transmission ($P(>N|B) < 0.0014$) in at least 9 consecutive pixels. The blue vertical lines mark individual transmission spikes. The troughs (regions between blue-shaded areas with length $L \geqslant 10$ cMpc) are indicated with arrows.

definition of the troughs depends on the 9 pixel averaged $P(>N|B)$, and thus, the trough lengths are measured at $\sim$1 cMpc accuracy. The troughs are truncated by transmitting or invalid spectral regions, e.g., geocoronal emission, which we take into account in the following analysis. The He II Lyα effective optical depth is $\tau_{\rm eff} = -\ln\langle f_\lambda/E_\lambda\rangle_L$, where $\langle\rangle_L$ is the average over the trough length L. In practice, we used the maximum likelihood method in the Poisson regime to measure $\tau_{\rm eff}$ (see W19 or M21 for details). We caution that due to our definition, troughs do not have a lower limit on $\tau_{\rm eff}$. Thus, $\tau_{\rm eff}$ can be measured in troughs at high significance even if small-scale spikes remain undetectable. In order to exclude possible individual strong He II Lyα absorption lines (column density $N_{\rm He\,II} \gtrsim 10^{19}\,{\rm cm}^{-2}$) from our trough measurements, we only consider lengths $L \geqslant 10$ cMpc. We emphasize that our trough measurement method depends on our ability to detect transmission spikes via $P(>N|B)$, and thus, the low S/N spectra will generally contain more and longer troughs. Therefore, physical inferences require detailed forward modeling (Section 4.1).

3.2. Observational Results

Figures 2–4 illustrate the results of our spike and trough measurements in the valid spectral regions. Additionally as an example, Figure 5 shows the $z > 3$ transmission spikes toward HS 0911+4809 in more detail. Table 2 lists all measured troughs with their redshift ranges, lengths, and effective optical depths. As expected, all four sight lines probing $z < 2.7$ show an emerging He II forest. The He II Lyα transmission rarely reaches unity, indicating strong He II absorption from underdense regions in the IGM that hampers fits to individual absorption lines based on the coeval H I Lyα forest (Reimers et al. 1997; Kriss et al. 2001; Fechner & Reimers 2007; McQuinn & Worseck 2014; Syphers & Shull 2014). Only four short troughs ($L \lesssim 30$ cMpc) are detected at $z < 2.72$, exclusively in the low S/N spectra and therefore subject to data quality.

At $2.72 < z < 3$ the He II Lyα absorption becomes patchy, i.e., there are alternating regions with clustered transmission spikes separated by longer troughs. This patchy He II absorption is most prominent toward HE 2347−4342 (Reimers et al. 1997), but persists to $z \sim 2.9$–3 toward HS 0911+4809 and Q 0302−003, shown here for the first time (Figure 3). The frequency of He II Lyα transmission spikes dramatically decreases toward higher redshifts. At $3 \lesssim z \lesssim 3.3$ we measure occasional and often isolated transmission spikes separated by $L \gtrsim 40$ cMpc long troughs in four sight lines (Figures 3 and 4). The trough lengths appear to increase with increasing redshift as expected due to the higher IGM He II fraction before the completion He II reionization (e.g., Compostella et al. 2013). The longest detected He II Lyα troughs (442 cMpc toward HE2QS J2311−1417 and 383 cMpc toward HE2QS J1630+0435) were already briefly mentioned in M21.

At $z > 3$, the rare He II transmission spikes typically arise from highly underdense regions of the IGM (McQuinn 2009) or highly ionized quasar proximity zones. Indeed, some of the spikes are very close to the background quasar proximity zones (e.g., Q1602+576 and Q0302−003), the sizes of which are likely underestimated due to their simple observational definition (Khrykin et al. 2016). Nevertheless, the inclusion of small regions with likely nonnegligible quasar influence does not strongly affect our analysis. Likewise, some of the transmission spikes might be caused by the transverse proximity effect of foreground quasars (Schmidt et al. 2017, 2018). However, only one sight line in our sample (Q0302+003) has confirmed foreground quasars that are likely associated with the transmission feature at $z \sim 3.05$ (Jakobsen et al. 2003; Schmidt et al. 2017).

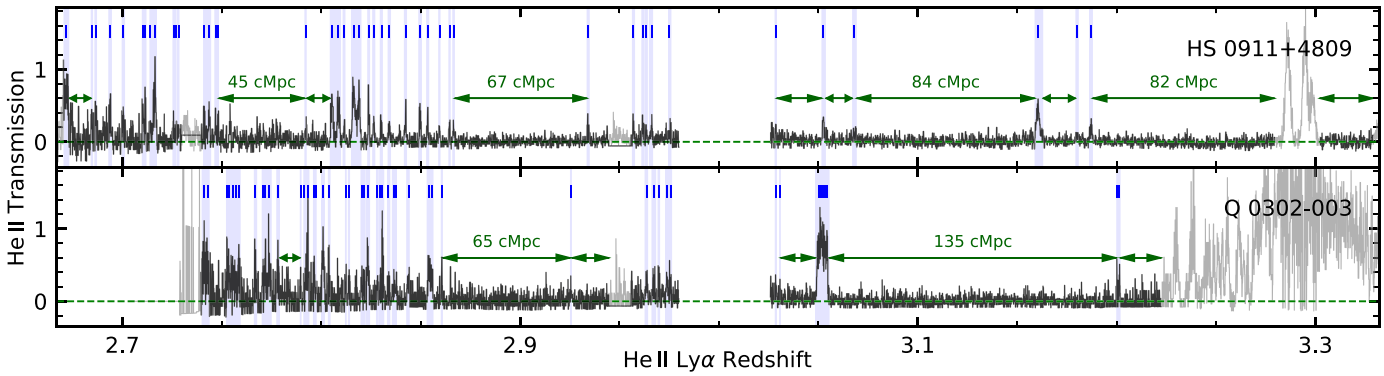

Figure 3. Similar to Figure 2, but for sight lines at $z_{\rm em} = 3.2$–3.5. Spectral regions with geocoronal Lyα λ1216, O I λ1304, N I λ1200, and N I λ1134 emission are omitted from the analysis.

Our measurements disregard the mostly weak absorption from the low-redshift H I Lyα forest overlapping with $z > 3$ He II Lyα absorption. This is justified because it is very unlikely that rare saturated H I absorption lines will black out rare He II transmission spikes.[8] Moreover, our ability to detect transmission spikes depends on the S/N, i.e., low S/N spectral regions naturally contain fewer spikes. The effects of the spectral quality on our measurements are addressed by forward-modeled mock spectra.

4. Comparison to a Hydrodynamical Simulation

4.1. Generation of Realistic Mock Spectra

Following our procedure in M21, we use realistic forward-modeled mock spectra from a numerical simulation, applying different models for the He II photoionization rate $\Gamma_{\rm He\,II}$ (i.e., a spatially constant UV background with varying amplitude, and a spatially fluctuating UV background). Only the comparison of the observational data to the mock spectra makes it possible to constrain the He II reionization history using the transmission spikes and troughs. With this, we quantify the UV background in terms of $\Gamma_{\rm He\,II}$ similar to D17 and W19.

For the mock spectra we used skewers from W19, which had been created from the outputs of a cubic $(146\,{\rm cMpc})^3$ hydrodynamical simulation run with the Nyx code (Almgren et al. 2013; Lukić et al. 2015) using the photoheating and photoionization rates from Haardt & Madau (2012). For every skewer, the He II Lyα optical depth was computed by using the velocity, temperature, and rescaled density $\rho \propto (1+z)^3$ fields from the outputs of the simulation at redshifts $z_{\rm sim} = 2.2$, 2.4, 2.5, 2.6, 3, 3.5, and 4. W19 created 1000 $\Delta z = 0.08$ (60–100 cMpc) long skewers in steps of $dz = 0.04$ between $z = 2.28$ and 3.88.

In order to capture long troughs comparable to our observations, we constructed unique $2.28 \leqslant z \leqslant 3.88$ synthetic spectra by splicing random skewers. The skewers were spliced at the points of the same $\tau_\alpha(z)$ and similar derivatives $d\tau_\alpha/dz$ in the $\Delta z = 0.04$ long overlapping regions. In this way, we avoid discontinuities in $\tau_\alpha(z)$ between the skewers. Since observationally there must be no strong Lyman limit systems along any of the He II-transparent quasar sight lines, we excluded skewers with H I Lyα optical depths $\tau_{\rm H\,I} > 3000$, which correspond to H I column densities $N_{\rm H\,I} \gtrsim 10^{17.1}\,{\rm cm}^{-2}$. In this way, we created 1000 unique $2.28 \leqslant z \leqslant 3.88$ synthetic spectra with a pixel size of 2–3 km s^{-1} each containing 39 spliced skewers with an average length of $\Delta z \sim 0.04$.

Assuming photoionization equilibrium in the optically thin limit, we rescaled the optical depths of the created spectra as $\tau_\alpha \propto \Gamma^{-1}_{\rm HeII}$ according to three sets of models: (1) a spatially fluctuating redshift-dependent $\Gamma_{\rm He\,II}$ (D17), (2) a spatially uniform $\Gamma_{\rm He\,II}$ that decreases with redshift as the median $\Gamma_{\rm He\,II}(z)$ from D17, and (3) a set of spatially uniform $\Gamma_{\rm He\,II}$ with variable amplitude $(10^{-16}\,{\rm s}^{-1} \leqslant \Gamma_{\rm He\,II} \leqslant 10^{-13}\,{\rm s}^{-1}$ with step size $\Delta[\log(\Gamma_{\rm He\,II}/{\rm s}^{-1})] = 0.1)$. The fluctuating UV background model from D17 showed excellent agreement with the measured $\tau_{\rm eff}$ distribution at $z < 3.3$, although it is in modest tension with the data at $z > 3.5$ (W19). The model was created using $(500\,{\rm cMpc})^3$ volume with an analytic IGM absorber model applying the H I column density distribution model from Prochaska et al. (2014) and the quasar luminosity function from Hopkins et al. (2007). The semi-analytical approach with approximate radiative transfer resulted in a spatially varying mean free path of ionizing photons, manifesting itself in the fluctuating UV background and consequently $\Gamma_{\rm He\,II}$. Here, we use a more recent simulation run from D17 with a slightly higher resolution of $(7.8\,{\rm cMpc})^3$ per grid cell in comparison to $(10\,{\rm cMpc})^3$ used in D17. For comparison, we also used a simplified model of a uniform UV background that decreases with redshift according to the median $\Gamma_{\rm He\,II}(z)$ from D17. This model captures the general redshift evolution of $\Gamma_{\rm He\,II}$, which is expected due to the redshift evolution of the quasar luminosity function (e.g., Hopkins et al. 2007; Kulkarni et al. 2019b; Puchwein et al. 2019).

Similar to (M21), we infer $\Gamma_{\rm He\,II}$ by comparing the incidence of spikes in the observed and mock data on large spatial scales of 150 cMpc. Here, we use the set of uniform UV background models (M21). By doing so, we neglect spatial fluctuations in the UV background, which is justified because our 150 cMpc scale is much larger than the mean free path of He II-ionizing photons at these redshifts (D17). This set of uniform UV background models is used only in Sections 4.3.1 and 4.3.2.

For all used UV background models the 1000 synthetic spectra were forward-modeled to resemble the observed spectra. For this, we applied the wavelength-dependent HST/COS G130M line-spread function to the transmission $e^{-\tau_\alpha}$, rebinned it to the wavelength grid of the observed spectra and

[8] At redshifts $z_{\rm H\,I} < 0.2$, corresponding to $z = 3.0$–3.8 for He II, there are on average $\simeq$5 H I absorbers with $\log N_{\rm H\,I} = 14$–17 (Kim et al. 2021) per line of sight. Each of these absorbers has an optical depth at the Lyα line center $\tau_{\rm H\,I} > 1.7$ and FWHM $\sim$0.3 Å after accounting for the COS line-spread function. The probability that at least one transmission spike overlaps with a Lyα absorption line is $\sim$0.6%–6%, depending on the number of spikes (1–10).

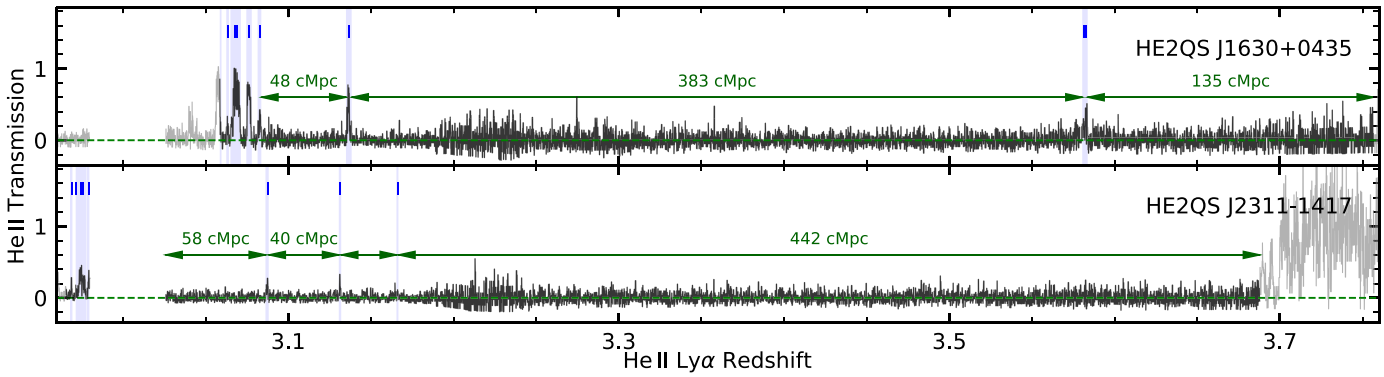

Figure 4. Similar to Figures 2 and 3, but for the two sight lines at $z_{em} > 3.5$. Spectral regions at the short-wavelength end are omitted due to He II Lyβ absorption.

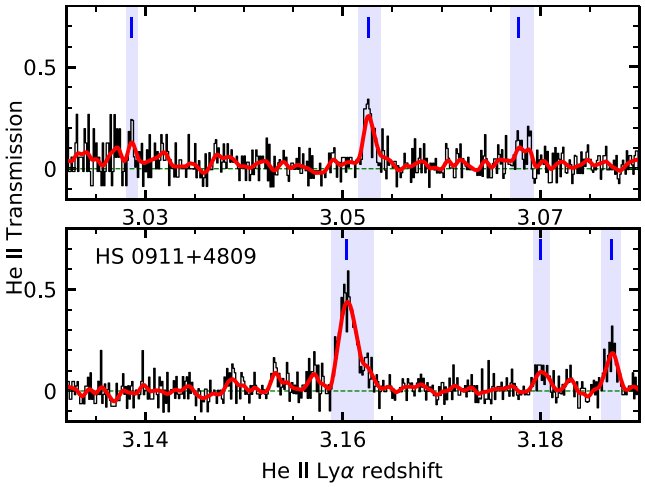

Figure 5. Similar to Figures 2–4, but zoomed-in on the $z > 3$ transmission spikes toward HS 0911+4809. The red line shows the transmission smoothed with a Gaussian filter ($\sigma_f = 0.1$ Å).

used the continuum, calibration curve, pixel exposure time and background to transform the transmission into expected counts per pixel. Measured counts were simulated by adding Poisson noise according to the expected counts per pixel. The resulting 1000 mock spectra per quasar sight line and model fully resemble the observational data in spectral resolution and quality including data gaps, enabling a one-to-one comparison.

4.2. He II Trough Length Distribution

For the fluctuating $\Gamma_{\rm He\,II}$ model and the median $\Gamma_{\rm He\,II}(z)$ from D17 we measured the trough lengths in the 1000 noise-free synthetic spectra to determine their redshift evolution without any observational effects. This means that we model the HST/COS count distributions from the transmission by using simplified wavelength-independent sensitivity curves, exposure times, and dark currents to calculate $P(>N|B)$, but we do not add Poisson noise to them. The results are presented in Figure 6. For the purpose of this plot, we defined the redshift position of the troughs as the midpoint in redshift Δz. The stripe in the upper right corner of both lower panels is due to the truncation of the troughs at the highest redshift of the synthetic spectra ($z = 3.88$). At $z > 3.3$, the uniform UV background model has such a low amplitude ($\Gamma_{\rm He\,II} \lesssim 10^{-15.4}\,{\rm s}^{-1}$) that only very long troughs are produced, which disagrees with the observations. Due to the midpoint definition of the troughs this results in a gap at $z \sim 3.4$. The fluctuating $\Gamma_{\rm He\,II}$ model provides a more realistic redshift evolution of the troughs with a wide range of trough lengths even at the highest redshifts.

Due to the small number of observed troughs (33 out of which 16 are at $z > 3$), it is not possible to capture their redshift evolution in detail. Instead, we investigated the distribution of troughs (number and lengths) separately at high ($z > 3$) and low ($z < 3$) redshift. Figure 7 shows the probability density functions (PDFs) of the number of troughs per mock sample (eight spectra) for the

Table 2
Measured Troughs with Length L and Effective Optical Depth $\tau_{\rm eff}$

Sight Line	Δz	L [cMpc]	$\tau_{\rm eff}$
HS 1700+6416	...	...	...
HS 1024+1849	2.691–2.722	33	$3.87^{+0.46}_{-0.31}$
	2.723–2.734	12	$2.99^{+0.27}_{-0.21}$
	2.741–2.757	17	>4.84
Q1602+576	2.590–2.600	12	>3.52
	2.610–2.619	10	>3.97
	2.798–2.810	13	>5.88
HE 2347−4342	2.752–2.767	15	>7.63
	2.769–2.788	20	>8.02
	2.789–2.799	10	$5.96^{+0.20}_{-0.16}$
	2.825–2.860	33	>8.56
Q0302−003	2.779–2.789	11	$2.91^{+0.27}_{-0.21}$
	2.861–2.925	65	$4.11^{+0.22}_{-0.18}$
	2.926–2.945	19	$4.71^{+1.02}_{-0.50}$
	3.031–3.048	17	$3.30^{+0.17}_{-0.14}$
	3.056–3.200	135	$5.63^{+0.58}_{-0.37}$
	3.202–3.222	18	>5.05
HS 0911+4809	2.673–2.684	12	$3.70^{+1.13}_{-0.52}$
	2.749–2.792	46	$3.64^{+0.20}_{-0.17}$
	2.793–2.804	12	$3.96^{+0.57}_{-0.36}$
	2.867–2.934	67	$6.05^{+4.26}_{-0.66}$
	3.029–3.052	22	$3.78^{+0.23}_{-0.18}$
	3.054–3.067	13	$3.82^{+0.28}_{-0.22}$
	3.069–3.159	84	$4.90^{+0.32}_{-0.24}$
	3.163–3.179	15	$4.76^{+0.67}_{-0.39}$
	3.188–3.279	82	>6.31
	3.302–3.329	23	$5.22^{+1.30}_{-0.57}$
HE2QS J2311−1417	3.026–3.086	58	$5.49^{+0.67}_{-0.39}$
	3.088–3.131	40	$4.78^{+0.33}_{-0.25}$
	3.132–3.166	31	$5.30^{+0.75}_{-0.42}$
	3.167–3.688	442	>6.83
HE2QS J1630+0435	3.084–3.135	48	$5.37^{+1.28}_{-0.54}$
	3.138–3.580	383	>6.57
	3.584–3.757	135	$5.76^{+2.23}_{-0.65}$

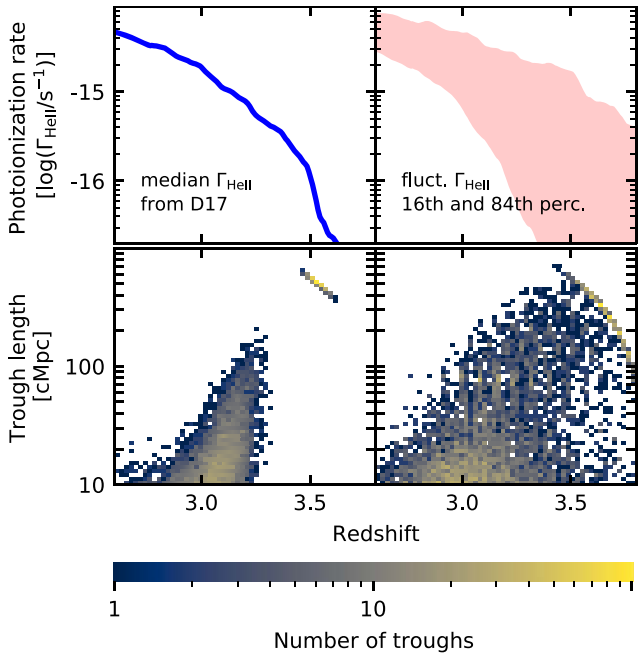

Figure 6. Redshift evolution of $\Gamma_{\rm He\,II}$ (upper panels) and the predicted number of troughs and their lengths (lower panels) in noise-free synthetic spectra for the spatially uniform $\Gamma_{\rm He\,II}$ model (left) and the fluctuating $\Gamma_{\rm He\,II}$ model (right). The stripe in the top right corner is caused by the redshift boundary of our synthetic spectra, naturally limiting the measured lengths of the troughs.

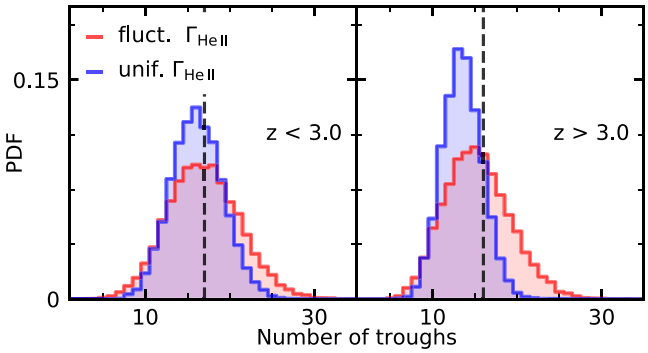

Figure 7. PDFs of the number of troughs with $L \geqslant 10$ cMpc in 10,000 sample realizations at $z < 3$ and $z > 3$. Results for the D17 fluctuating UV background model are shown in red, while those for a spatially uniform median $\Gamma_{\rm He\,II}(z)$ from D17 are shown in blue. The number of detected troughs in the observed sample are indicated with the dashed lines.

two $\Gamma_{\rm He\,II}$ models. For this, we used 10,000 sample realizations of the mock data. Both models are consistent with the measured number of troughs given our data. Given the width and similarity of the predicted distributions, the number of troughs is insufficient to distinguish between the two models.

While the number of troughs does not evolve with redshift, the troughs are becoming significantly longer with increasing redshift. Figure 8 shows the cumulative distribution functions (CDFs) of the trough lengths for the observed (Table 2) and the mock spectra. For the computation of the CDFs from mocks, we selected sample realizations with the same number of troughs as in the observed data ($m = 17$ at $z < 3$ and $m = 16$ at $z > 3$). This selection is required, because the distribution of trough lengths changes with the number of troughs whose lengths are constrained by the total available path length.

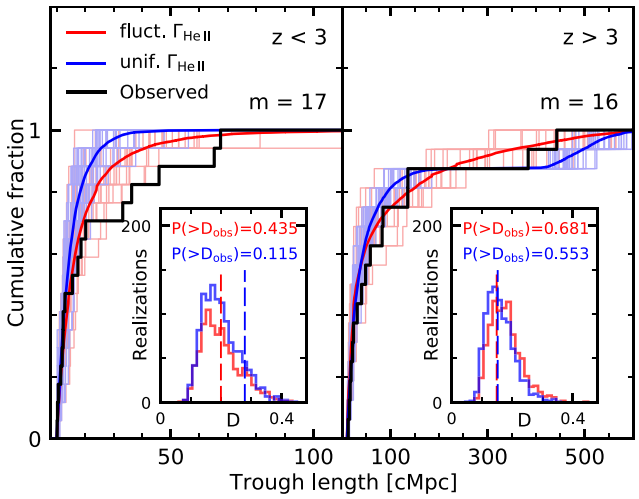

Figure 8. CDFs of the trough lengths in the observed sample (black) and in the respective mock samples (red: spatially fluctuating $\Gamma_{\rm He\,II}$; blue: spatially uniform $\Gamma_{\rm He\,II}(z)$). The solid red and blue lines were constructed from 10,000 sample realizations using all samples with $m = 17$ troughs at $z < 3.0$ (left panel) and $m = 16$ at $z > 3.0$ (right panel). The pale blue and red lines show 25 representative realizations for the respective models. The inset shows the distributions of the K-S test statistic D for the CDFs of the individual realizations and the CDF of all samples. The dashed lines mark the values $D_{\rm obs}$ for the observed data and all samples. $P(>D_{\rm obs}) > 0.1$ indicates that the observed data is consistent with both models at the 0.1 significance level.

At $z < 3$, the modeled CDFs do not seem to match the observed CDF, due to the five $L > 30$ cMpc troughs. For the fluctuating $\Gamma_{\rm He\,II}$ model, only ~3% of our sample realizations have at least five $L > 30$ cMpc troughs, while there are almost none for the uniform $\Gamma_{\rm He\,II}$ model. At $z > 3$, both models agree with the observed data. Given our sample size and quality, the modeled CDFs are too close to be distinguishable.

We performed a two-sample Kolmogorov–Smirnov (K-S) test to quantitatively compare the observed data to the models. First, we computed the K-S test statistic D (absolute maximum distance between two CDFs) for each CDF from the individual sample realizations (pale colors in Figure 8) and the CDF of all sample realizations (dark colors). The resulting distributions of D for each model are shown in the insets of Figure 8. Then, by calculating the fraction of $D > D_{\rm obs}$ where $D_{\rm obs}$ is the K-S test statistic between the observed data and the model, we estimated the probability $P(>D_{\rm obs})$ that the model is consistent with the observations. At any redshift both models cannot be rejected ($P(>D_{\rm obs}) > 0.1$). However, for the uniform UV background model at $z < 3$, none of the mock samples features as many long troughs (30 cMpc $\lesssim L \lesssim$ 70 cMpc) as the observations. A closer investigation reveals that the calculated K-S test statistic is dominated by sample variance at $L \lesssim 20$ cMpc. The PDFs and CDFs recalculated for $L \geqslant 20$ cMpc do not change significantly at $z > 3$. At $z < 3$, however, the comparison of the PDFs in Figure 9 clearly favors the fluctuating UV background model. Nevertheless, the CDFs of both models are not consistent with the observations owing to the small probability $P(>D_{\rm obs}) < 0.04$. The formal rejection of the D17 fluctuating UV background model suggests that the UV background might fluctuate on larger scales (or stronger) than predicted by D17. Overall, short troughs with $L \lesssim 20$ cMpc that occur frequently and may be impacted by density fluctuations hamper the model distinction, similar to Zhu et al. (2021) for H I.

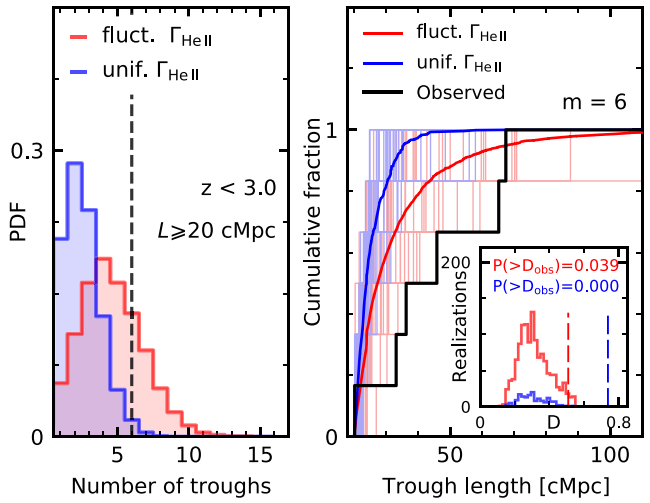

Figure 9. Similar to Figures 7 and 8, but for $L \geqslant 20$ cMpc at $z < 3$.

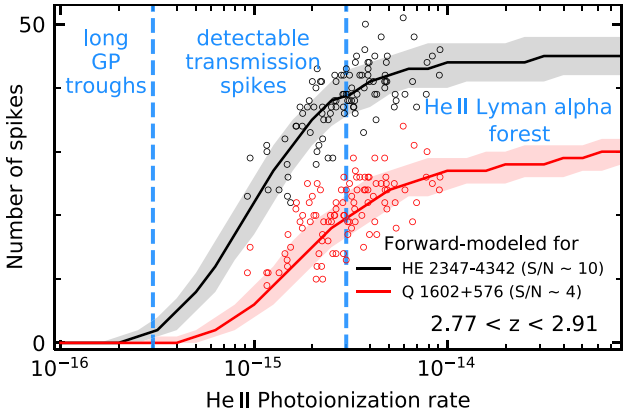

Figure 10. Increase in the number of He II Lyα transmission spikes with increasing photoionization rate $\Gamma_{\rm He\,II}$ in 1000 mock spectra at $2.77 < z < 2.91$ (150 cMpc) at spectral quality of HE 2347−4342 (black) and Q1602+576 (red). The lines show the median number of spikes for an assumed spatially uniform $\Gamma_{\rm He\,II}$ with their respective 84th and 16th percentiles (shades). The circles show the measured number of spikes in 100 representative mock spectra with the fluctuating UV background model plotted at the respective median $\Gamma_{\rm He\,II,D17}$ of the skewer. Here, many more transmission spikes are measured toward HE 2347−4342 due to the higher S/N.

4.3. Inference of the He II Photoionization Rate

4.3.1. Incidence of Spikes Depends on $\Gamma_{He\,II}$

We showed in M21 that the incidence of transmission spikes can be used to infer the volume-weighted median He II photoionization rate. As a representative example, Figure 10 shows how the number of spikes increases with increasing $\Gamma_{\rm He\,II}$ for mock spectra of two quasars with different data quality in the redshift range $z = 2.77$–2.91 (150 cMpc) with the spatially uniform (lines) and fluctuating (circles) UV background models. For the uniform $\Gamma_{\rm He\,II}$ model, the graph can be roughly divided in three regions. At $\Gamma_{\rm He\,II} \lesssim 3 \times 10^{-16}\,{\rm s}^{-1}$, there are only a few spikes, and the spectra are dominated by troughs. Then at $\Gamma_{\rm He\,II} \gtrsim 3 \times 10^{-16}\,{\rm s}^{-1}$, spikes become more frequent, first in the most underdense regions. Here, the number of spikes increases monotonically. The curve reaches a plateau at $\Gamma_{\rm He\,II} \sim (3$–$6) \times 10^{-15}\,{\rm s}^{-1}$, as the number of detectable spikes at a given data quality saturates. At higher $\Gamma_{\rm He\,II}$, the mock spectra become predominantly transmitting, showing an emerging He II Lyα forest. The plot shows that the incidence of spikes is very sensitive to the He II photoionization rate $\Gamma_{\rm He\,II}$ in the regime of detectable transmission spikes. The small variance comes mainly from IGM density fluctuations and Poisson noise in the mock spectra.

To show the dependence of the spike incidence on a fluctuating $\Gamma_{\rm He\,II}$ in Figure 10, we used 100 representative mock spectra for the same sight lines and redshift bin. In Figure 10, we plot the calculated median He II photoionization rate per sight line $\Gamma^{\rm los}_{\rm He\,II,D17}$ and the measured number of spikes for each of these mock spectra. The range of $\Gamma^{\rm los}_{\rm He\,II,D17}$ is predefined by the fixed model and thus, does not cover the full range of our custom uniform $\Gamma_{\rm He\,II}$ models. The number of spikes increases with increasing $\Gamma^{\rm los}_{\rm He\,II,D17}$ in a similar manner and with similar scatter as the uniform UV background models. The range of $\Gamma^{\rm los}_{\rm He\,II,D17}$ changes with redshift but always follows the curves for the spatially uniform UV background models. Therefore, approximating the fluctuating UV background with a set of uniform models is well justified on our adopted large scale of 150 cMpc.

4.3.2. Inference of $\Gamma_{He\,II}$ for the Uniform UV Background

Similar to M21, we used the number of transmission spikes in predefined redshift bins to infer the photoionization rate $\Gamma_{\rm He\,II}$. For this, we calculated the likelihood $\mathcal{L}(n|\Gamma_{\rm He\,II})$ from the PDFs of the number of spikes n in fixed 150 cMpc long redshift bins using our mock spectra for the set of uniform UV background models. Then by using Bayes' theorem, we constructed a normalized posterior

$$p_{\Delta z,i}(\Gamma_{\rm He\,II}|n_i) \propto \mathcal{L}_{\Delta z,i}(n_i|\Gamma_{\rm He\,II})p(\Gamma_{\rm He\,II}) \quad (2)$$

given the number of detected spikes n_i in the redshift bin Δz along the sight line i using a flat prior $p(\Gamma_{\rm He\,II})$ in the range of our UV background models ($10^{-16}\,{\rm s}^{-1} \leqslant \Gamma_{\rm He\,II} \leqslant 10^{-13}\,{\rm s}^{-1}$). The calculations were performed for every sight line and redshift bin that has usable data in $\geqslant 30\%$ of the bin ($\geqslant 45$ cMpc). The used bins size of 150 cMpc ensures a good sampling of transmission spikes (especially a concern at $z > 3$) while tracking the redshift evolution of the He II photoionization rate. Their positions were chosen to maximize the usable spectral coverage, resulting in eight redshift bins at $2.5 \leqslant z \leqslant 3.76$.

The top panels of Figures 11 and 12 show the resulting posteriors. Since there are no spikes detected at $3.22 \leqslant z < 3.57$ along any of the sight lines, the posteriors provide only upper limits on $\Gamma_{\rm He\,II}$. Here, we are in the regime of long troughs where the He II photoionization rate at these redshifts must be $\Gamma_{\rm He\,II} \lesssim 2 \times 10^{-15}\,{\rm s}^{-1}$ given our data. A good example of an opposite extreme case is at $z = 2.63$–2.77 toward HS 1700+6416. Here, we are in the He II Lyα forest regime (the plateaus at high $\Gamma_{\rm He\,II}$ values in Figure 10) where the detected number of spikes is not sensitive to the photoionization rate anymore. Only two other posteriors show this behavior, at $z = 2.50$–2.63 toward HE 2347−4342 and at $z = 2.77$–2.91 toward HS 1024+1849.

Most of the posteriors are well defined, providing inferences of the photoionization rate. The positions of the posteriors at the same redshift sometimes varies substantially, exceeding expectations from IGM density fluctuations that dominate the widths of individual posteriors. This is further evidence for a fluctuating UV background, possibly down to $z \sim 2.6$.

We inferred the median photoionization rate $\Gamma_{\rm He\,II}$ in every redshift bin from the joint posterior

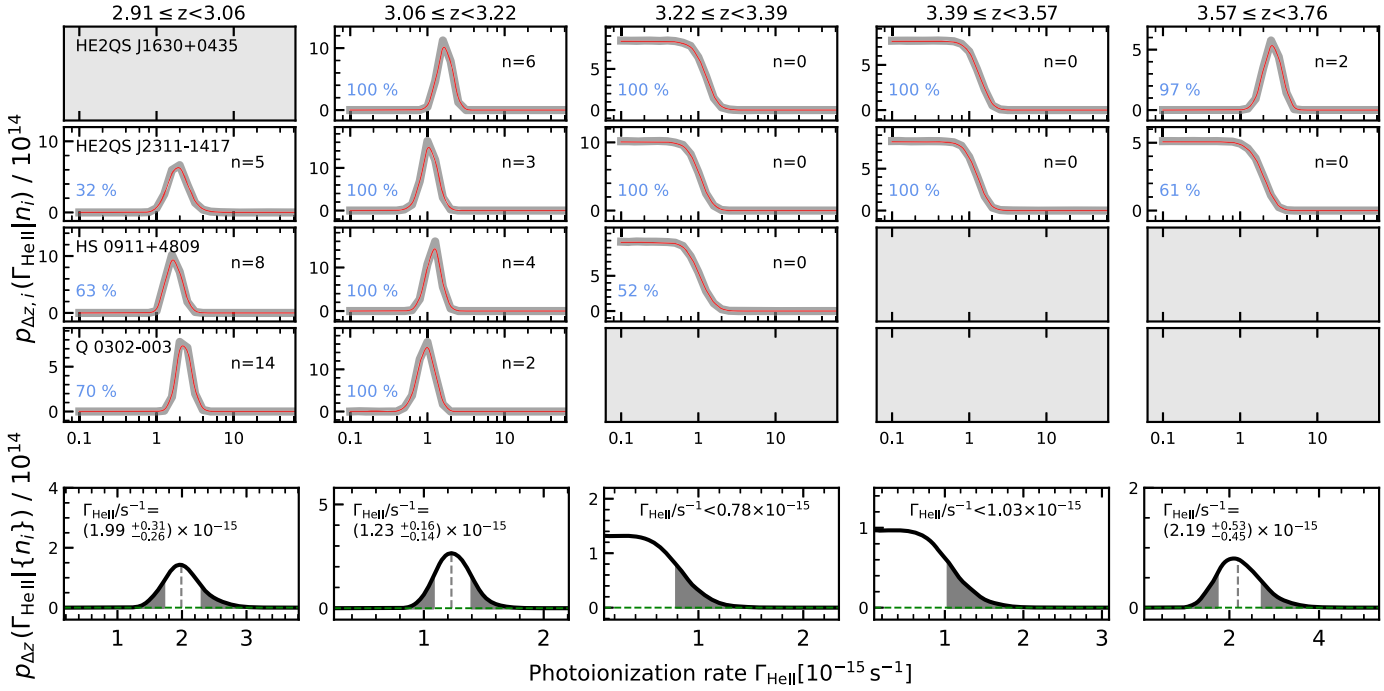

Figure 11. Top: normalized posteriors $p_{\Delta z,i}(\Gamma_{\rm He\,II}|n_i)$ for 150 cMpc long redshift bins at $z \geqslant 2.91$. The posteriors sampled at $\Delta \log(\Gamma_{\rm He\,II}/{\rm s}^{-1}) = 0.1$ are shown in gray. Final results were obtained after smoothing and subsampling them with a Gaussian kernel ($\sigma = 0.05 \times 10^{-15}$ s^{-1}, red). The grayed out panels indicate discarded redshift bins (usable data in <30% of the bin, i.e., <45 cMpc). In all other panels we indicate the fractional data coverage. Bottom: joint posteriors $p_{\Delta z}(\Gamma_{\rm He\,II}|\{n_i\})$. Vertical dashed lines indicate the posterior median while the gray areas mark the tails below the 16th and above the 84th percentile, yielding the measurements and statistical uncertainties of $\Gamma_{\rm He\,II}$, respectively.

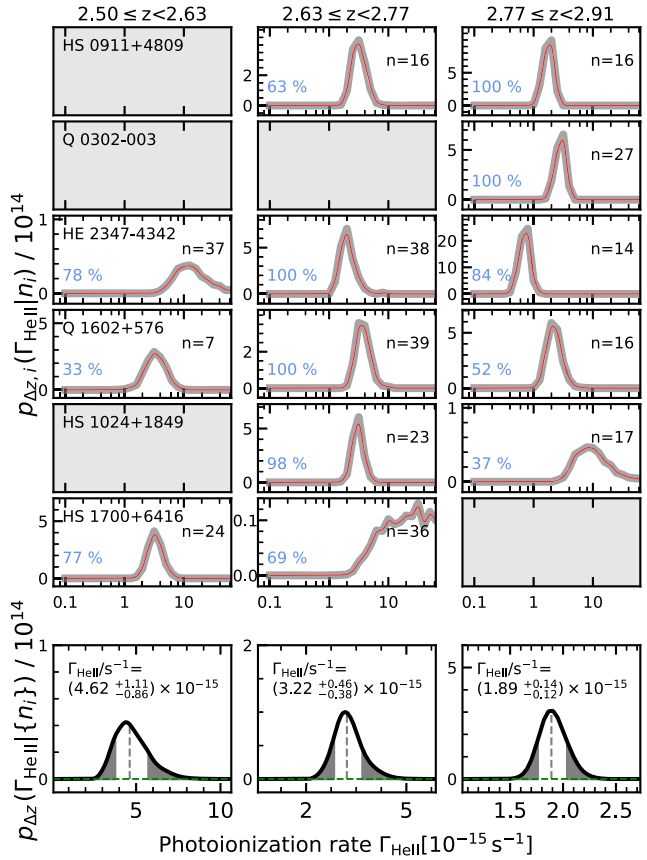

Figure 12. Similar to Figure 11, but for redshift bins at $z \leqslant 2.91$.

$$p_{\Delta z}(\Gamma_{\rm He\,II}|\{n_i\}) \propto \prod_i p_{\Delta z,i}(\Gamma_{\rm He\,II}|n_i). \quad (3)$$

To ensure a good sampling of $p_{\Delta z}(\Gamma_{\rm He\,II}|\{n_i\})$ we smoothed and subsampled the individual posteriors with a $\sigma = 0.05 \times 10^{-15}\,{\rm s}^{-1}$ Gaussian kernel to reduce effects of partial overlap over the $\Gamma_{\rm He\,II}$ range. A single joint posterior distribution estimates the most probable He II photoionization rate along all contributing sight lines for our assumed uniform UV background. We quote the median of $p_{\Delta z}$ (Figures 11 and 12, bottom panel) as our measurement of $\Gamma_{\rm He\,II}$, while the 16th and 84th percentile yield the equal-tailed 1σ uncertainty. For the redshift bins without detected transmission spikes we quote the 84th percentile as the 1σ upper limit. Table 3 lists the resulting photoionization rates $\Gamma_{\rm He\,II}$.

4.3.3. Inference of $\Gamma_{\rm He\,II}$ for the Fluctuating UV Background

Although the approximation of a uniform UV background along individual sight lines is well justified (see Section 4.3.1), it might be too strong for the inference of $\Gamma_{\rm He\,II}$ from the joint posterior. As a result, this joint posterior may lead to unrealistic constraints on $\Gamma_{\rm He\,II}$. To test whether the joint posterior yields a representative value for the more realistic fluctuating UV background from D17, we inferred $\Gamma_{\rm He\,II}$ for each of the 1000 sample realizations in our defined redshift bins. Then we compared the inferred $\Gamma_{\rm He\,II}$ to the known median photoionization rate $\Gamma^{\rm med}_{\rm He\,II,D17}$ in the same sample realizations by calculating $\delta_\Gamma = \Gamma_{\rm He\,II}/\Gamma^{\rm med}_{\rm He\,II,D17}$. We caution that $\Gamma^{\rm med}_{\rm He\,II,D17}$ can vary from sample to sample, i.e., it is not the overall median He II photoionization rate used in Section 4.2.

Table 3
Inferred He II Photoionization Rates ($\Gamma_{\rm He\,II}$) in Redshift Bins Δz from s Sight Lines with a Total Path Length d

Δz	$\Gamma_{\rm He\,II}(10^{-15}\,{\rm s}^{-1})$	d (cMpc)	s
2.50–2.63	$4.62^{+1.11}_{-0.86}$	280	3
2.63–2.77	$3.22^{+0.46}_{-0.38}$	655	5
2.77–2.91	$1.89^{+0.14}_{-0.12}$	559	5
2.91–3.06	$1.99^{+0.31}_{-0.26}$	258	3
3.06–3.22	$1.23^{+0.16}_{-0.14}$	600	4
3.22–3.39	$\leqslant 0.78$	379	3
3.39–3.57	$\leqslant 1.03$	300	2
3.57–3.76	$2.19^{+0.53}_{-0.45}$[a]	237	2

Note.
[a] Unreliable.

Figure 13 shows the median δ_Γ with its 16th–84th percentile range. At $z<3$ the inferred $\Gamma_{\rm He\,II}$ agrees with the input $\Gamma^{\rm med}_{\rm He\,II,D17}$ to within a small scatter, showing that Equation (3) is still applicable to a fluctuating UV background. At $z>3$, however, the He II photoionization rate is systematically overestimated. A closer investigation shows that the bias appears if the joint likelihood is computed for spectra with and without spikes (i.e., at $3.57\leqslant z<3.76$ in Figure 11). In these cases, the $n>0$ posterior will always narrow the joint posterior, whereby the lower $\Gamma_{\rm He\,II}$ values from the $n=0$ posteriors are effectively ignored. This artificially increases the inferred $\Gamma_{\rm He\,II}$, such that $\Gamma_{\rm He\,II}$ is representative only for ionized (i.e., transmissive) regions of the IGM. Due to the dropping D17 He II photoionization rate the bias strongly increases with redshift. This bias can be somewhat mitigated by a higher S/N, such that transmission spikes are detectable in many spectra (Figure 13). It completely disappears if all spectra show transmission spikes ($3.06\leqslant z<3.22$ in Figure 13).

The combination of $n>0$ and $n=0$ posteriors in or data appears only in the highest-redshift bin ($3.57\leqslant z<3.76$), making this measurement unreliable. Due to the well-defined posteriors at $z<3.22$, our procedure yields the median $\Gamma_{\rm He\,II}$ also in the case of a fluctuating UV background. In Table 3, we list the inferred $\Gamma_{\rm He\,II}$ values, which correspond to the sample median $\Gamma_{\rm He\,II}$ of the contributing observed sight lines.

4.4. Redshift Evolution of the He II Photoionization Rate

Figure 14 shows the redshift evolution of the inferred He II photoionization rates in comparison to previously published measurements by W19 and to the fluctuating UV background model by D17. The He II photoionization rate strongly decreases from $z\simeq 2.5$ to $z\simeq 3.2$, and likely even at higher redshifts, as indicated by our upper limits on $\Gamma_{\rm He\,II}$. As previously mentioned, the measurement at $z\sim 3.7$ is considered untrustworthy due to the strong bias uncertainties and thus, it will not be discussed further.

For the comparison to the predicted $\Gamma_{\rm He\,II}$ from the D17 model, we considered the strong variance from our limited sample size. For this, we computed the sample medians $\Gamma^{\rm med}_{\rm He\,II,D17}$ from corresponding subsamples of the 1000 D17 $\Gamma_{\rm He\,II}$ skewers (Section 4.1). The violins in Figure 14 show the distribution of 1000 calculated $\Gamma^{\rm med}_{\rm He\,II,D17}$ values, indicating that substantial scatter from sample variance is expected. Our inferences are in very good agreement with the D17 model given the expected sample variance, except at $z\simeq 2.8$. The reason for the outlier at $z\simeq 2.8$ is the unusual low-transmission spectrum of HE 2347−4342 (Figures 2 and 12). In particular, the 36 cMpc long trough at $z\sim 2.83$ is difficult to reproduce in He II reionization models, possibly indicating a very rare region with a still significant He II fraction (e.g., Furlanetto & Dixon 2010; Shull et al. 2010). The exclusion of this sight line from our small sample results in $\Gamma_{\rm He\,II}=(2.53^{+0.34}_{-0.27})\times 10^{-15}\,{\rm s}^{-1}$ at $z\simeq 2.8$ making it consistent with D17.

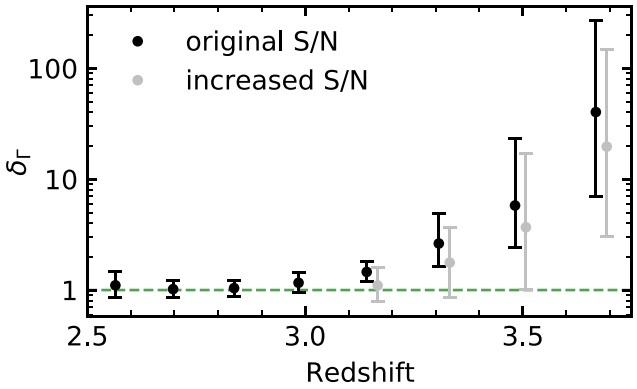

Figure 13. Median ratio between the measured photoionization rate $\Gamma_{\rm He\,II}$ and the median $\Gamma_{\rm He\,II,D17}$, $\delta_\Gamma=\Gamma_{\rm He\,II}/\Gamma^{\rm med}_{\rm He\,II,D17}$ (black), as determined from 1000 mock sample realizations. Gray symbols show the case for an increased S/N ∼ 15–30 at the highest redshifts.

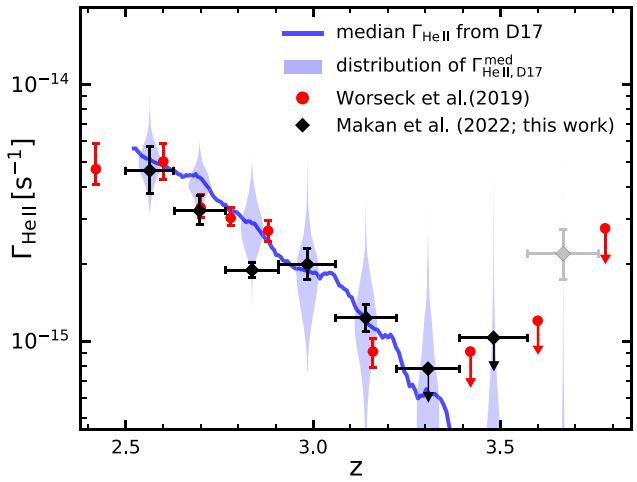

Figure 14. Redshift evolution of the He II photoionization rate $\Gamma_{\rm He\,II}$ inferred from the incidence of transmission spikes (black) and from the He II effective optical depth (red, W19). The unreliable inference at $z\sim 3.7$ is shown in gray. The line indicates the median $\Gamma_{\rm He\,II,D17}$ while the violins show the distribution of the sample medians $\Gamma^{\rm med}_{\rm He\,II,D17}$ from 1000 sample realizations.

Figure 14 also shows the $\Gamma_{\rm He\,II}$ inferences from the effective optical depth measurements by W19. Our measurements are in broad agreement with W19, with the largest difference at $z\simeq 2.8$ due to the particular sight line of HE 2347−4342. Additionally, unlike W19, we are able to measure $\Gamma_{\rm He\,II}$ at $z\sim 3$ owing to the longer spectral coverage and the negligible scattered light around geocoronal Lyα in our G130M data.

5. Summary

We have systematically analyzed small-scale and large-scale He II Lyα absorption features (transmission spikes and absorption troughs) in eight high-resolution ($R\simeq$ 12,500–18,000) HST/COS spectra. This is the first comprehensive sample of high-resolution

He II absorption spectra probing the end of the He II reionization epoch at $2.50 < z < 3.76$. We measured trough lengths and the incidence of spikes using the automated routine established in (M21). Then, we compared our measurements to predictions from forward-modeled mock spectra from a hydrodynamical simulation employing different UV background models.

We measured 33 troughs (i.e., $L \geqslant 10$ cMpc regions without significant small-scale transmission), 16 of which are at $z > 3$. While the number of troughs is similar at $z < 3$ and $z > 3$, their length dramatically increases with increasing redshift. There are six 82 cMpc $\leqslant L \leqslant$ 442 cMpc troughs at $z > 3$, whereas each trough at $z < 3$ spans $\lesssim$65 cMpc. The distribution of trough lengths at $z < 3$ is in disagreement with the predictions from a spatially uniform UV background and the (D17) fluctuating UV background model, suggesting that the UV background might fluctuate on even larger scales than predicted by D17. At $z > 3$, our measured trough length distribution cannot rule out the tested models, although the UV background is naturally expected to fluctuate strongly at these redshifts (Figure 7).

We used the incidence of transmission spikes to infer He II photoionization rate $\Gamma_{\rm He\,II}$ similar to M21. For this we compared the measured incidence to predictions from a $(146\,{\rm cMpc})^3$ hydrodynamical simulation for a wide range of $\Gamma_{\rm He\,II}$. The inferred $\Gamma_{\rm He\,II}$ decreases with increasing redshift from $\simeq 4.6 \times 10^{-15}\,{\rm s}^{-1}$ at $z \simeq 2.6$ to $\simeq 1.2 \times 10^{-15}\,{\rm s}^{-1}$ at $z \simeq 3.2$, in agreement with the D17 fluctuating UV background model (Figure 14). At $3.22 < z < 3.57$, the lack of transmission spikes results in upper limits $\Gamma_{\rm He\,II} \lesssim 10^{-15}\,{\rm s}^{-1}$ that are still in agreement with D17. At these high redshifts we find that our measurement technique overestimates the IGM He II photoionization rate because it is dominated by transmission spikes that probe rare highly ionized regions. We have identified such a case at the highest redshifts probed here ($3.57 \geqslant z < 3.76$). Conversely, due to the limited sensitivity of the He II Lyα absorption to high He II fractions, the troughs may be produced by large incompletely ionized regions similar to the suggested H I *neutral islands* at $z \sim 5.5$ (Malloy & Lidz 2015; Kulkarni et al. 2019a; Keating et al. 2020). Detailed comparisons to our data require refined numerical simulations with a broad range of He II reionization histories.

We conclude that the incidence of transmission spikes is sensitive to the He II photoionization rate (Figure 10) and yields similar values as the He II effective optical depth from larger but lower-resolution samples (W19). On the other hand, we have shown that the trough statistics require a much larger sample to distinguish between different plausible models of He II reionization and/or the fluctuating He II-ionizing background. This is similar to the situation of H I at $z \simeq 6$ where the trough statistics had been used early on (Songaila & Cowie 2002; Fan et al. 2006; Gallerani et al. 2006), but only recently they had the ability to distinguish between reionization models in larger samples (Zhu et al. 2021). Given the substantial HST/COS exposure times and the generally faint background quasars, a significant increase of the sample requires a next-generation large UV space telescope (e.g., The LUVOIR Team 2019). A 6–8 m UV-sensitive space telescope, as recently prioritized in the Decadal Survey on Astronomy and Astrophysics 2020 (National Academies of Sciences, Engineering, and Medicine 2021), would be able to gather high-resolution $R \simeq 20{,}000$ spectra of more than 20 $m_{\rm FUV} = 21$–22 quasars discovered with HST (Syphers et al. 2012; Worseck et al. 2019). Such observations would statistically determine the evolution of the He II absorption from individual high-redshift transmission spikes to a resolved He II Lyα forest.

We thank the anonymous referee for the constructive review. This work was funded by Bundesministerium für Wirtschaft und Energie in the framework of the Verbundforschung of the Deutsches Zentrum für Luft- und Raumfahrt (DLR, grant 50 OR 1813). Support for program GO 15356 was provided by NASA through a grant from the Space Telescope Science Institute, which is operated by the Association of Universities for Research in Astronomy, Inc., under NASA contract NAS5-26555. This research is based on observations made with the NASA/ESA Hubble Space Telescope obtained from the Space Telescope Science Institute, which is operated by the Association of Universities for Research in Astronomy, Inc., under NASA contract NAS 526555. These observations are associated with programs GTO 11528, GTO 12033, GO 12816, GO 13301, and GO 15356.

Facility: HST (COS).

Software: astropy (Astropy Collaboration et al. 2013, 2018), SciPy (Virtanen et al. 2020), matplotlib (Hunter 2007), NumPy (Harris et al. 2020).

ORCID iDs

Kirill Makan https://orcid.org/0000-0003-3157-1191
Gábor Worseck https://orcid.org/0000-0003-0960-3580
Frederick B. Davies https://orcid.org/0000-0003-0821-3644
Joseph F. Hennawi https://orcid.org/0000-0002-7054-4332
J. Xavier Prochaska https://orcid.org/0000-0002-7738-6875
Philipp Richter https://orcid.org/0000-0002-1188-1435

References

Almgren, A. S., Bell, J. B., Lijewski, M. J., Lukić, Z., & Van Andel, E. 2013, ApJ, 765, 39
Astropy Collaboration, Price-Whelan, A. M., Sipőcz, B. M., et al. 2018, AJ, 156, 123
Astropy Collaboration, Robitaille, T. P., Tollerud, E. J., et al. 2013, A&A, 558, A33
Barnett, R., Warren, S. J., Becker, G. D., et al. 2017, A&A, 601, A16
Becker, G. D., Bolton, J. S., Madau, P., et al. 2015, MNRAS, 447, 3402
Boera, E., Murphy, M. T., Becker, G. D., & Bolton, J. S. 2014, MNRAS, 441, 1916
Bosman, S. E. I., Davies, F. B., Becker, G. D., et al. 2021, arXiv:2108.03699
Cardelli, J. A., Clayton, G. C., & Mathis, J. S. 1989, ApJ, 345, 245
Chardin, J., Haehnelt, M. G., Bosman, S. E. I., & Puchwein, E. 2018, MNRAS, 473, 765
Choudhury, T. R., Paranjape, A., & Bosman, S. E. I. 2021, MNRAS, 501, 5782
Compostella, M., Cantalupo, S., & Porciani, C. 2013, MNRAS, 435, 3169
Compostella, M., Cantalupo, S., & Porciani, C. 2014, MNRAS, 445, 4186
Davies, F. B., Furlanetto, S. R., & Dixon, K. L. 2017, MNRAS, 465, 2886
Eide, M. B., Ciardi, B., Graziani, L., et al. 2020, MNRAS, 498, 6083
Eilers, A.-C., Hennawi, J. F., Davies, F. B., & Oñorbe, J. 2019, ApJ, 881, 23
Fan, X., Strauss, M. A., Becker, R. H., et al. 2006, AJ, 132, 117
Fardal, M. A., Giroux, M. L., & Shull, J. M. 1998, AJ, 115, 2206
Faucher-Giguère, C.-A., Lidz, A., Hernquist, L., & Zaldarriaga, M. 2008, ApJ, 688, 85
Fechner, C., & Reimers, D. 2007, A&A, 461, 847
Feldman, G. J., & Cousins, R. D. 1998, PhRvD, 57, 3873
Furlanetto, S. R., & Dixon, K. L. 2010, ApJ, 714, 355
Furlanetto, S. R., & Oh, S. P. 2008, ApJ, 681, 1
Gaikwad, P., Rauch, M., Haehnelt, M. G., et al. 2020, MNRAS, 494, 5091
Gallerani, S., Choudhury, T. R., & Ferrara, A. 2006, MNRAS, 370, 1401
Gallerani, S., Ferrara, A., Fan, X., & Choudhury, T. R. 2008, MNRAS, 386, 359
Garaldi, E., Gnedin, N. Y., & Madau, P. 2019, ApJ, 876, 31
Gnedin, N. Y., Becker, G. D., & Fan, X. 2017, ApJ, 841, 26
Green, J. C., Froning, C. S., Osterman, S., et al. 2012, ApJ, 744, 60
Haardt, F., & Madau, P. 2012, ApJ, 746, 125

Harris, C. R., Millman, K. J., van der Walt, S. J., et al. 2020, Natur, 585, 357
Hiss, H., Walther, M., Hennawi, J. F., et al. 2018, ApJ, 865, 42
Hopkins, P. F., Richards, G. T., & Hernquist, L. 2007, ApJ, 654, 731
Hu, W., Wang, J., Zheng, Z.-Y., et al. 2019, ApJ, 886, 90
Hunter, J. D. 2007, CSE, 9, 90
Jakobsen, P., Boksenberg, A., Deharveng, J. M., et al. 1994, Natur, 370, 35
Jakobsen, P., Jansen, R. A., Wagner, S., & Reimers, D. 2003, A&A, 397, 891
Keating, L. C., Weinberger, L. H., Kulkarni, G., et al. 2020, MNRAS, 491, 1736
Khrykin, I. S., Hennawi, J. F., McQuinn, M., & Worseck, G. 2016, ApJ, 824, 133
Khrykin, I. S., Hennawi, J. F., & Worseck, G. 2019, MNRAS, 484, 3897
Kim, T. S., Wakker, B. P., Nasir, F., et al. 2021, MNRAS, 501, 5811
Kriss, G. A., Shull, J. M., Oegerle, W., et al. 2001, Sci, 293, 1112
Kulkarni, G., Keating, L. C., Haehnelt, M. G., et al. 2019a, MNRAS, 485, L24
Kulkarni, G., Worseck, G., & Hennawi, J. F. 2019b, MNRAS, 488, 1035
La Plante, P., Trac, H., Croft, R., & Cen, R. 2017, ApJ, 841, 87
Lukić, Z., Stark, C. W., Nugent, P., et al. 2015, MNRAS, 446, 3697
The LUVOIR Team 2019, arXiv:1912.06219
Madau, P., Haardt, F., & Rees, M. J. 1999, ApJ, 514, 648
Madau, P., & Meiksin, A. 1994, ApJL, 433, L53
Makan, K., Worseck, G., Davies, F. B., et al. 2021, ApJ, 912, 38
Malloy, M., & Lidz, A. 2015, ApJ, 799, 179
Mason, C. A., Treu, T., Dijkstra, M., et al. 2018, ApJ, 856, 2
McQuinn, M. 2009, ApJL, 704, L89
McQuinn, M., Lidz, A., Zaldarriaga, M., et al. 2009, ApJ, 694, 842
McQuinn, M., & Worseck, G. 2014, MNRAS, 440, 2406
Meiksin, A. 2020, MNRAS, 491, 4884
Miralda-Escude, J. 1993, MNRAS, 262, 273
Miralda-Escudé, J., Haehnelt, M., & Rees, M. J. 2000, ApJ, 530, 1
Møller, P., & Jakobsen, P. 1990, A&A, 228, 299
Morrissey, P., Conrow, T., Barlow, T. A., et al. 2007, ApJS, 173, 682
Murthy, J. 2014, ApJS, 213, 32
National Academies of Sciences, Engineering, and Medicine 2021, Pathways to Discovery in Astronomy and Astrophysics for the 2020s (Washington, DC: The National Academies Press) https://www.nap.edu/catalog/26141/pathways-to-discovery-in-astronomy-and-astrophysics-for-the-2020s
Paschos, P., & Norman, M. L. 2005, ApJ, 631, 59
Picard, A., & Jakobsen, P. 1993, A&A, 276, 331
Planck Collaboration, Aghanim, N., Akrami, Y., et al. 2020, A&A, 641, A6
Prochaska, J. X., Madau, P., O'Meara, J. M., & Fumagalli, M. 2014, MNRAS, 438, 476
Puchwein, E., Haardt, F., Haehnelt, M. G., & Madau, P. 2019, MNRAS, 485, 47
Reimers, D., Kohler, S., Wisotzki, L., et al. 1997, A&A, 327, 890
Schlegel, D. J., Finkbeiner, D. P., & Davis, M. 1998, ApJ, 500, 525
Schmidt, T. M., Hennawi, J. F., Worseck, G., et al. 2018, ApJ, 861, 122
Schmidt, T. M., Worseck, G., Hennawi, J. F., Prochaska, J. X., & Crighton, N. H. M. 2017, ApJ, 847, 81
Shull, J. M., France, K., Danforth, C. W., Smith, B., & Tumlinson, J. 2010, ApJ, 722, 1312
Shull, M., & Danforth, C. 2020, arXiv:2007.02948
Sokasian, A., Abel, T., & Hernquist, L. 2002, MNRAS, 332, 601
Songaila, A., & Cowie, L. L. 2002, AJ, 123, 2183
Syphers, D., Anderson, S. F., Zheng, W., et al. 2009a, ApJS, 185, 20
Syphers, D., Anderson, S. F., Zheng, W., et al. 2009b, ApJ, 690, 1181
Syphers, D., Anderson, S. F., Zheng, W., et al. 2012, AJ, 143, 100
Syphers, D., & Shull, J. M. 2014, ApJ, 784, 42
Virtanen, P., Gommers, R., Oliphant, T. E., et al. 2020, NatMe, 17, 261
Walther, M., Oñorbe, J., Hennawi, J. F., & Lukić, Z. 2019, ApJ, 872, 13
Worseck, G., Davies, F. B., Hennawi, J. F., & Prochaska, J. X. 2019, ApJ, 875, 111
Worseck, G., Khrykin, I. S., Hennawi, J. F., Prochaska, J. X., & Farina, E. P. 2021, MNRAS, 505, 5084
Worseck, G., & Prochaska, J. X. 2011, ApJ, 728, 23
Worseck, G., Prochaska, J. X., Hennawi, J. F., & McQuinn, M. 2016, ApJ, 825, 144
Worseck, G., Prochaska, J. X., McQuinn, M., et al. 2011, ApJL, 733, L24
Yang, J., Wang, F., Fan, X., et al. 2020, ApJ, 904, 26
Zhu, Y., Becker, G. D., Bosman, S. E. I., et al. 2021, ApJ, 923, 223